JOURNAL OF GEOPHYSICAL RESEARCH: PLANETS, VOL. 118, 908–915, doi:10.1002/jgre.20079, 2013

Convection-driven compaction as a possible origin of Enceladus's long wavelength topography

J. Besserer,[1] F. Nimmo,[1] J. H. Roberts,[2] and R. T. Pappalardo[3]

Received 16 November 2012; revised 14 February 2013; accepted 8 April 2013; published 6 May 2013.

[1] The long wavelength surface topography of Enceladus shows depressions about 1 km in depth and $\sim 10^2$ km wide. One possible cause of this topography is spatially variable amounts of compaction of an initially porous ice shell, driven by spatial variations in heat flux. Here, we show that the heat flux variations associated with convection in the shell can quantitatively match the observed features. We develop a simple model of viscous compaction that includes the effect of porosity on thermal conductivity, and find that an initial shell porosity of at least 20–25% is required to develop the observed topography over $\sim$ 1 Ga. This mechanism produces topographic depressions, not rises, above convective upwellings, and does not generate detectable gravity anomalies. Unlike transient dynamic topography, it can potentially leave a permanent record of ancient convective processes in the shallow lithospheres of icy satellites.

Citation: Besserer, J., F. Nimmo, J. H. Roberts, and R. T. Pappalardo (2013), Convection-driven compaction as a possible origin of Enceladus's long wavelength topography, *J. Geophys. Res. Planets*, *118*, 908–915, doi:10.1002/jgre.20079.

1. Introduction

[2] Saturn's icy moon Enceladus is a puzzling body that exhibits a surprising level of (localized) activity in relation to its small diameter of $\sim$ 504 km. Its surface displays a variety of characteristics that may be clues to unravelling both its present state and its evolution [e.g., *Spencer et al.*, 2009]. For instance, global long-wavelength topography shows several quasi-circular depressions about 0.8–1.5 km in depth and 90–75 km wide [*Schenk and McKinnon*, 2009; *Nimmo et al.*, 2011]. A slightly wider depression is associated with the South Polar Terrain, which is also the source of thermal and jet activity [*Porco et al.*, 2006; *Spencer et al.*, 2006] and which may be caused by locally reduced shell thickness and an underlying regional sea [*Collins and Goodman*, 2007].

[3] Such a regional liquid layer may be able to sufficiently decouple the ice shell from the silicate-metal core [*Tobie et al.*, 2008] that tidal heating and/or thermal convection could be focused in the overlying ice shell [*Běhounková et al*., 2012]. Elsewhere, current thermal convection (if any) in Enceladus's ice shell seems to be marginal [e.g., *Barr and McKinnon*, 2007] and a global ocean would crystallize in a few tens of million years [*Roberts and Nimmo*, 2008b; *Spencer et al.*, 2009]. One possibility is that there have been periodic episodes of localized activity and/or melting [*Ojakangas and Stevenson*, 1986; *Meyer and Wisdom*, 2008], consistent with the existence of different terrains with different inferred ages [*Spencer et al.*, 2009]. A long-term globally convecting Enceladus also appears difficult to reconcile with orbital constraints [*Zhang and Nimmo*, 2009], but localized, episodic convective activity cannot be ruled out.

[4] A key characteristic of the basins discovered by *Schenk and McKinnon* [2009] lies in their spatial distribution: these features all appear to be uncorrelated with any geological boundary. This suggests a deep internal source for their origin. Therefore, investigating the formation mechanism of these basins may help unravel part of Enceladus's thermal history. The most plausible mechanism is isostasy [*Schenk and McKinnon*, 2009], either from shell thickness variations (i.e., Airy isostasy) driven by deep thermal anomalies (at the core surface, or of tidal origin), or from density variations (i.e., Pratt isostasy). However, a tidal mechanism seems difficult to reconcile with the basins' spatial distribution, while shell thickness variations are difficult to maintain against lateral flow [*Stevenson*, 2000]. Density variations are a more promising mechanism to account for these basins. *Schenk and McKinnon* [2009] conclude that such topographic lows could be either the surface expression of cold, denser regions of a clathrate-enriched ice shell (see also section 4), or the result of porosity reduction by annealing due to localized, enhanced heat fluxes. In this paper, we will quantify this second possibility for the case in which convection is responsible for spatial variations in heat flux and thus compaction. In particular, the effect of the evolving porosity on thermal conductivity is taken into account [*Shoshany et al.*, 2002], resulting in a feedback between viscous compaction and thermal evolution [e.g., *Eluszkiewicz*, 1990; *Castillo-Rogez et al.*, 2007]. If such a mechanism

[1]Department of Earth and Planetary Sciences, University of California, Santa Cruz, California, USA.
[2]Johns Hopkins University Applied Physics Laboratory, Laurel, Maryland, USA.
[3]Jet Propulsion Laboratory, California Institute of Technology, Pasadena, California, USA.

Corresponding author: J. Besserer, Department of Earth and Planetary Sciences, University of California, 1156 High Street, Santa Cruz, CA 95064, USA. (jbessere@ucsc.edu)

2169-9097/13/10.1002/jgre.20079

Table 1. Ice Shell Physical Parameters Used in This Study

Symbol	Name	Value
L	Thickness of the conductive layer	25 km
d	Total thickness the ice shell	70–88 km
R_E	Outer radius	250 km
ρ_I	Density	920 kg · m^{-3}
c_p	Specific heat[a]	2.1 kJ · K^{-1} · kg^{-1}
k_I	Thermal conductivity[b]	3 W · m^{-1} · K^{-1}
ϕ_p	Percolation limit	0.7
$\phi_{\min}$	Microporosity	0.01
(a, b)	Conductivity factors	(4.1, 0.22)
ϕ_0	Initial porosity	0.05–0.30
D	Grain size	0.01–10 mm
g	Gravity acceleration	0.112 m · s^{-2}

[a] Some simulations were conducted with a temperature-dependent specific heat: $c_p(T) = 7.49T + 90$ J · K^{-1} · kg^{-1} [*Klinger*, 1981]. See text for a discussion.

[b] Some simulations were also conducted with a temperature-dependent thermal conductivity: $k(\phi, T) = k(\phi)/k_I \times K(T)$ [see equation (2a)], with $K(T) = 567/T$ W · m^{-1} · K^{-1} [*Klinger*, 1980]. See text for a discussion.

ever occurred, the associated topographic depressions could be direct surface "trace fossils" of past activity inside the ice shell.

2. Methodology

[5] The model consists of a thin, initially porous layer of thickness L, being the near-surface, conductive part of Enceladus's ice shell, characterized by an outer radius R_E. The values of the different parameters used in this study are given in Table 1. Temperature evolution is governed by the energy conservation equation:

$$\frac{\partial T}{\partial t} = \frac{1}{\rho c_p} \nabla \cdot (k \nabla T), \tag{1}$$

where T is the temperature, t is the time, $\rho \equiv (1 - \phi)\rho_I$ is the effective density of the medium, with ϕ the porosity and ρ_I the density of ice, c_p is its specific heat (here constant), and k is the thermal conductivity. The latter property strongly varies with porosity. This dependence is considered here through the two bounding expressions derived by *Shoshany et al.* [2002]:

$$k_{\text{low}}(\phi) \equiv k(\phi) = k_I \left(1 - \frac{\phi}{\phi_p}\right)^{a\phi + b}, \tag{2a}$$

$$k_{\text{up}}(\phi) = k_{\text{low}}(\phi_{\min})^{\ln(1-\phi)/\ln(1-\phi_{\min})}, \tag{2b}$$

where k_I is the thermal conductivity of compact ice (i.e., $\phi = 0$), ϕ_p is a percolation limit, a and b are constant factors [*Shoshany et al.*, 2002], and $\phi_{\min}$ is the microporosity of the medium (here taken to be 1%). Note that the precise value of the microporosity has a minor influence on the thermal conductivity. One uniquely realistic aspect of the approach of *Shoshany et al.* [2002] is that it allows for a distribution of pore sizes [see *Prialnik et al.*, 2004, for a review]. Although we generally assume that conductivity is governed by equation (2a), we discuss how using equation (2b) modifies our results in sections 3 and 4.

[6] Viscous flow tends to remove the porosity, according to the following equation [*Fowler*, 1985; *Nimmo et al.*, 2003]:

$$\frac{\partial \ln \phi}{\partial t} = -\frac{P}{\eta}, \tag{3}$$

where P is the overburden pressure and η the effective dynamic viscosity of the ice. The approach used by *Eluszkiewicz* [2004] is slightly more complicated but produces very similar results (see section 3).

[7] Because only the shallow part of the ice shell is considered in the present study, gravitational acceleration g can reasonably be considered constant, and tidal heat production can be neglected. The overburden pressure is then obtained by directly integrating the density column $\rho(\phi)$. The effective viscosity is described according to the semi-empirical composite law of *Goldsby and Kohlstedt* [2001], yielding:

$$\eta(T, \sigma, D) \equiv \left[\eta_{\text{diff}}^{-1} + \eta_{\text{disl}}^{-1} + \left(\eta_{\text{bas}} + \eta_{\text{gbs}}\right)^{-1}\right]^{-1}, \tag{4}$$

where σ is differential stress, D is grain size (constant in this study), and the subscripts diff, disl, bas, and gbs refer to the various mechanisms contributing to viscous deformation of ice, namely diffusion flow, dislocation creep, basal slip, and grain boundary sliding, respectively. The activation energies, pre-exponential factors, and grain size and stress exponents are those prescribed by *Goldsby and Kohlstedt* [2001, see their Tables 5 and 6]. Following *Eluszkiewicz* [1990, 2004], we assume that σ is given by the overburden pressure (because this pressure leads to deviatoric stresses at the grain boundaries).

[8] We model the porosity and thermal evolution by integrating in time coupled equations (1) and (3) with a simple explicit scheme. Equations are radially discretized through a 1D-spherical finite volume method (second order in space), on a staggered mesh of 100 radial cells (i.e., a spatial resolution of 250 m; see Table 1): discrete variables corresponding to T and η are defined at the center of the control volumes while those used for k, ϕ and ρ are defined on cell walls. In particular, this enables us to use the exact value of the time-dependent conductivity $k(\phi)$ (no interpolation needed) in the heat diffusion scheme; indeed, this is a key parameter in the coupled problem.

[9] The required surface boundary condition consists of a prescribed temperature that depends on latitude. The corresponding functions are given by *Ojakangas and Stevenson* [1989], and are scaled here to Enceladus's insolation conditions [e.g., *Roberts and Nimmo*, 2008b]. At the bottom of the ice layer, a laterally variable heat flux is imposed; the values are those generated by the 2D convection simulations of *Roberts and Nimmo* [2008a] and extend from north to the south pole of Enceladus. Two endmember cases were used: case 1 of *Roberts and Nimmo* [2008a] (convective ice shell thickness $d = 70$ km, reference viscosity of 3×10^{13} Pa · s) and an additional similar case that was run for $d = 88$ km. Tidal heating is included in these simulations [see *Roberts and Nimmo*, 2008b, for the method] and ice melting is taken into account. In the purely conductive shallow part of the stagnant lid that is considered here, tidal heating is negligible. The thickness L of this shallow layer (see Table 1) is chosen such that the bottom temperatures are sufficiently high to

prevent any long-term porosity, but sufficiently low that pure heat conduction remains a valid approximation. The precise value of L does not matter as long as the base of the initial layer corresponds to a depth where long-term porosity cannot be sustained. Therefore, the base of this layer always exceeds the depth to the base of the megaregolith (see also sections 3 and 4). The initial solution for the simulations consists of the analytical conductive profile characterizing a layer with a homogeneous initial porosity ϕ_0, a specified surface temperature and a basal heat flux. Porosity and thermal evolution are computed [equations (3) and (1)] for each of the 193 latitudinal locations used by *Roberts and Nimmo* [2008a]. The basal heat flux is assumed to be constant and the evolution calculations are carried out over a long timescale, typically 1 Ga. This timescale is grossly comparable to the inferred difference in ages between individual ancient terrains [*Kirchoff and Schenk*, 2009]. Because temperature variations (hence compaction by viscous flow) are predominantly radial in the stagnant lid, our approach reasonably approximates a full 2D-method.

[10] The thickness of the porous layer will change laterally as a result of lateral variations of the bottom heat flux, and, to a much lesser extent, due to the latitudinally varying surface temperature. The resulting variations in subsidence will create topography at the surface. After a given time, t_1 of evolution, the topography Δh relative to the north pole value (arbitrarily fixed at 0 here) is simply obtained, at a latitude λ, by the following equation:

$$\Delta h(t_1, \lambda) = \int_{R_E - L}^{R_E} [\, \phi(r, t_1; \lambda) - \phi(r, t_1; \pi/2) \,]\, \mathrm{d}r. \qquad (5)$$

3. Results

[11] As an illustrative example, Figure 1 shows some radial porosity distributions obtained after 1 Ga of evolution, and the corresponding temperature profiles. The initial porosity was here $\phi_0 = 0.2$ or $\phi_0 = 0.3$, and different values of the grain size D were considered: 0.1, 1, and 10 mm. The main feature observed is a sharp transition from a deep, pore-free region to a shallow porous outer layer of thickness 6–10 km. Such a structure is similar to the results of *Nimmo et al.* [2003, Figure 6], for the case of Jupiter's Galilean moon Europa, but the final thicknesses of the porous region are much higher in the case of Enceladus. This is due to a surface gravity that is 10 times smaller on Enceladus, and also to a lower thermal gradient; both enable porosity to persist to greater depths. In the *Nimmo et al.* [2003] approach, the temperature at the bottom of the shell, a constant thermal conductivity, and a Newtonian viscosity were prescribed. Here, we relax these simplifications. The porosity structures depicted in Figure 1a are also consistent with other studies that have used a similar approach [*Castillo-Rogez et al.*, 2007, for Iapetus], two-phase flow modeling [*Eluszkiewicz*, 1990, for Mimas], or compaction timescale estimates [*Eluszkiewicz*, 2004, for Europa].

[12] The thickness of the final porous layer chiefly depends on the initial porosity considered, since this quantity directly controls the shallow thermal gradient, and hence the depth at which porosity removal occurs, for given bottom heat flux and grain size. The result is a trade-off between the thickness of the final porous layer and the value of its initial porosity. An increase in grain size tends to increase the effective viscosity, and therefore decreases the rate of porosity removal [see equation (3)], explaining the range of depths observed in Figure 1a for the various values of D. For a grain size of 0.1 mm, grain size-sensitive (GSS) creep—here grain boundary sliding—is the dominant viscous flow mechanism in most parts of the compacting region of the porous layer, and dislocation creep (grain size-insensitive) only acts in the warmest (i.e., deepest) parts. However, increasing grain size widens the dislocation creep-dominated area, explaining the smaller and smaller changes in the porous layer thickness as the grain size approaches 10 mm. At this value, GSS creep is restricted to shallow depths (< 5 km).

[13] Figure 1a also displays a characteristic example (D = 10 mm, $\phi_0 = 0.3$) of a final porosity profile that was obtained using the formulation of *Eluszkiewicz* [1990, 2004]. In this case, $\partial\phi/\partial t$ is no longer proportional to ϕ, as in equation (3), but to a more complex function $f(\phi)$ that depends on the creep mechanism. The main result of using this formulation is a more gradual transition between the fully compacted and the porous regions. This is consistent with the shape of the profiles obtained in the case of Mimas [*Eluszkiewicz*, 1990]. However, the average depth of the transition region is close to the one obtained with the Fowler approach [see Figure 1a]. Consequently, the *relative* topography due to compaction [equation (5)] is almost unaffected, as we will see below. Hence, in the rest of this paper, we will continue to use the Fowler approach [i.e., equation (3)] because we will only consider a pure ice composition for Enceladus ice shell. Note that the presence of impurities, such as silicates and/or ammonia in the ice would require using more sophisticated empirical, parameterized compaction rules [*Leliwa-Kopystynski and Maeno*, 1993; *Leliwa-Kopystyński and Kossacki*, 1995].

[14] The associated thermal profiles [Figure 1b] are well described by conductive thermal equilibrium in a medium characterized by two different conductivities. Note that the bottom, fully compacted region of the conductive shell has a conductivity k_I ($3.0\ \mathrm{W \cdot m^{-1} \cdot K^{-1}}$), while the top porous layer is characterized by the value $2.1\ \mathrm{W \cdot m^{-1} \cdot K^{-1}}$ ($\phi \equiv 0.2$) or $1.3\ \mathrm{W \cdot m^{-1} \cdot K^{-1}}$ ($\phi \equiv 0.3$). In general, Figure 1 shows that the initial porosity is the most important parameter in determining the final thermal and porosity structures.

[15] The initial porosity of the ice layer strongly affects the thermal transfer (insulating effect), and consequently the viscous compaction-induced surface relief. This initial porosity is most likely the result of regolith generation via impacts occurring during and after accretion of the body. One of the few studies that modelled icy satellites regolith evolution is the work of *Eluszkiewicz* [1990]. This author found that a primordial initial surface porosity of 30–40% should characterize Mimas, together with a regolith depth of a few tens of kilometers ($\sim$ 10 km according to the study of *Leliwa-Kopystyński and Kossacki* [2000]). For Enceladus, *Kossacki and Leliwa-Kopystyński* [1993] obtained a post-accretional structure characterized by a 5–10 km thick porous shallow layer. Note that the authors fixed the surface porosity at 50% in their approach—a value that we argue was probably strongly affected by the subsequent evolution of the satellite (see section 4), for instance, its differentiation [*Schubert et al.*, 2007]. Experimental studies suggest that, for pressures of less than 5 MPa that characterize the first tens of kilometers of Enceladus's ice mantle, a porosity of at

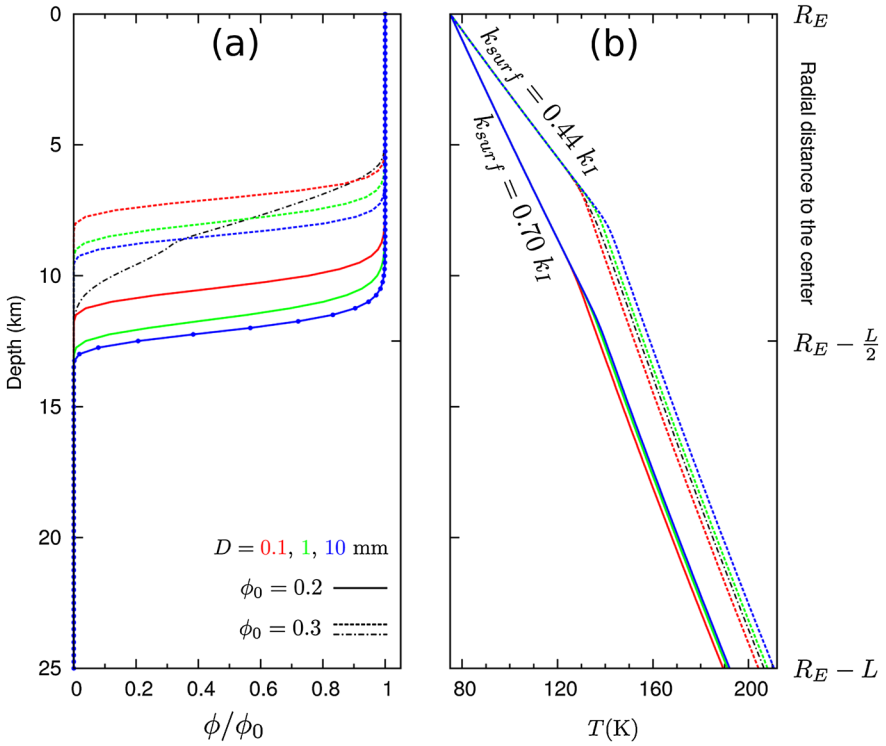

Figure 1. Examples of the structure obtained after a 1 Ga evolution. (a) Porosity structure, normalized to initial porosity. The different colors and line styles refer to various values of the grain size and initial porosity, respectively. For the curve corresponding to the case (D, ϕ_0) = (10 mm, 0.2), the points indicate the discretization, depicting the spatial resolution employed. Note the sharp transition (∼2.5–4 km) from a deep, fully compacted region to a shallow porous outer layer. The thin, dash-dotted curve was obtained through the approach of *Eluszkiewicz* [1990, see text], and corresponds to the case (D, ϕ_0) = (10 mm, 0.3). The slight slope change at $\phi = \phi_0/3$ is due to a change of behavior [i.e., discontinuity of the function $f(\phi)$] for $\phi < 0.1$ [*Eluszkiewicz*, 1990]. (b) Corresponding thermal profiles. In this case, the constant surface temperature and bottom heat flux are 75 K and 13.2 mW m^{-2}, respectively. Note also the different shallow thermal conductivity values k_{surf} (a fraction of the value k_I for compact ice) that correspond to each family of curves.

least 25% (and up to 35%) can be sustained at low temperatures [*Durham et al.*, 2005, $T < 120$ K]. Below we adopt an initial porosity range of 5–30% in the top 25 km, and discuss the extent to which such initial values are plausible in section 4.

[16] Figure 2 displays examples of results obtained for simulations with various values for the initial porosity ϕ_0 and grain size D when spatial variations in heat flux due to convection are taken into account. The colored curves in Figure 2 depict the effective surface topography obtained with our model, which is simply the sum of the compaction-induced topography and the dynamic topography induced by the underlying convection (black curve). The net topography is the superposition of two competing characteristics of convective upwellings. The buoyancy in the upwellings tends to deflect the shell upwards, but the enhanced heat flux leads to a shallower porous layer, promoting subsidence. In most cases the contribution from compaction dominates, with the exception of cases with initial porosities that are so low ($\leq$ 3.5%) that little compaction is possible. Therefore, convective upwellings lead to negative topography, a counterintuitive result.

[17] Neglecting subsequent porosity generation, these compaction-induced topographic lows will be permanent features. Thus, the long-wavelength depressions observed at Enceladus's surface are potentially "trace fossils" recording the location of ancient upwellings (see section 4). The topographic variations found with our model are characterized by a wavelength of $\sim$ 175 km, as a consequence of the hot/cold plumes distribution in the convective ice mantle. The maximal peak-to-peak variation of these profiles ranges from 80 m (ϕ_0 = 0.05, D = 0.01 mm) to 685 m (ϕ_0 = 0.30, D = 10 mm). Note that the corresponding values obtained after a shorter evolution timescale of 100 Ma are 90 and 750 m, respectively. The grain size-induced variations increase from 8% (ϕ_0 = 0.05) to 18% (ϕ_0 = 0.30). Hence, for this particular convection model, the amplitude and wavelength of the model topography achieve only $\sim$ half the values characterizing the observed basins on Enceladus [*Schenk and McKinnon*, 2009; *Nimmo et al.*, 2011]. Figure 2 also shows that the sole amplitude of the surface dynamic topography (< 100 m; bottom black curve) is too small (thick stagnant lid) to account for Enceladus's large basins, as predicted by *Schenk and McKinnon* [2009].

[18] However, for a thicker ice mantle (i.e., case with d = 88 km), we found a much better match between the observations of *Schenk and McKinnon* [2009] and our modelled surface topography. This is illustrated in Figure 3,

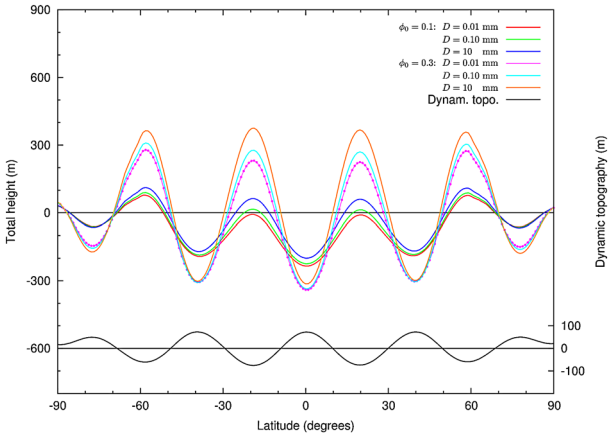

Figure 2. Topographic profiles obtained after a 1 Ga evolution in the case d = 70 km. The different colors refer to various values of the initial porosity ϕ_0 and of the grain size D. The curves represent the sum of the surface dynamic topography due to convection [*Roberts and Nimmo*, 2008a] and the surface topography due to compaction [equation (5)] (left vertical axis). The curve depicting the case (D, ϕ_0) = (0.01 mm, 0.3) includes points that indicate the horizontal discretization of our "2D"-model (i.e., resolution of $\sim$ 0.94°, or $\sim$ 4.1 km). The bottom black curve depicts the surface dynamic topography due to convection alone (right vertical axis). The heat flux at the base of the shallow porous layer ranges from 10 to 16 mW $\cdot$ m^{-2}. Due to its anti-correlation with the compaction-induced topography, the dynamic topography tends to reduce the effect of compaction, although such decrease remains minor in case of high initial porosity.

where three families of model profiles, obtained after 1 Ga, are compared with a North-South cross section of the most prominent basin found on the stereo-derived map of *Schenk and McKinnon* [2009, their basin A, labelled here on Figure 3]. Here the grain size is fixed at an intermediate value (D = 1 mm). In addition, the uncertainty in the pore size distribution is taken into account by using both equations (2a) and (2b)—the solid and dashed curves, respectively, in Figure 3. Because the sensitivity of thermal conductivity to porosity is much reduced in equation (2b) compared with equation (2a), the resulting range of results reflects not only possible lateral variations of the pore size distribution, but also our rather rough knowledge of the precise effect of porosity on thermal conductivity [*Prialnik et al.*, 2004]. In a more general point of view, the shaded area can also be seen as including other uncertainties, such as the topography-increasing effect of a temperature-dependent thermal conductivity (see section 4), etc. Note that the cases using equation (2b) display greater topographic amplitudes. This is due to the resulting lower temperature gradients that enable porosity to persist to greater depths, therefore increasing the differential compaction between regions of lower and higher heat fluxes.

[19] We compared our method to the more sophisticated approach of *Eluszkiewicz* [1990] and found the results to be similar. For instance, for the case displayed in Figure 1a [i.e., D = 10 mm, conductivity given by equation (2a)], the maximal peak-to-peak topographic amplitudes are increased by only 2.1% (ϕ_0 = 0.15) and < 0.6% (ϕ_0 > 0.20), respectively.

[20] Compared to the case with a thinner ice shell (d = 70 km), two factors result in an improved match with the observations when d is increased: (1) the longer wavelength arising from the thicker shell and (2) the larger lateral heat flux variations, a consequence of fewer and stronger plumes in the longer-wavelength convection regime. Note that, in this case, the convective solution showed slight time-dependence (a purely steady state was obtained for d = 70 km). As an illustrative example, Figure 3 shows the final topography obtained with a snapshot of the horizontal heat flux distribution at the base of the shallow porous layer. The data profile of *Schenk and McKinnon* [2009] has been horizontally and vertically shifted in Figure 3 to better emphasize the similarity with the modelled profiles (only relative elevations are displayed).

[21] Figure 3 suggests that the observed surface topography could be explained by convection-driven compaction of a shallow layer with an initial porosity of ~25–30%. The maximal peak-to-peak topographic amplitude obtained is 2120 m [ϕ_0 = 0.3, k given by equation (2b)]. For a shorter

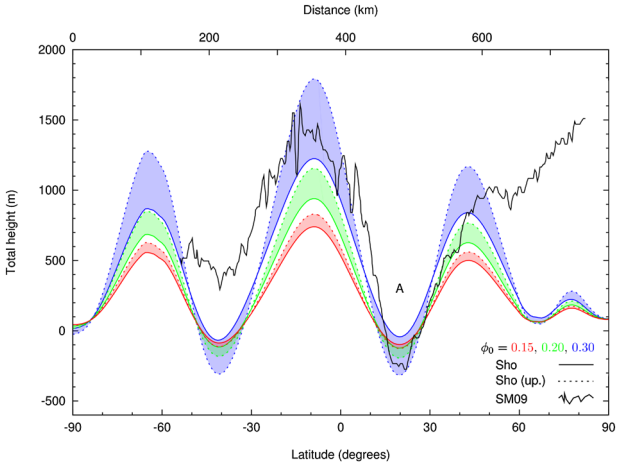

Figure 3. Comparison between observed and model topographic profiles obtained after a 1 Ga evolution in the case d = 88 km. The different colors refer to values of the initial porosity ϕ_0. The grain size is fixed at 1 mm. The curves represent the sum of the surface dynamic topography due to convection [*Roberts and Nimmo*, 2008a] (range of values is here –159 to +117 m) and the surface topography due to compaction [equation (5)]. The solid and dotted lines correspond to the thermal conductivity given by equations (2a) and (2b), respectively; the area between the curves defines the likely range of possible values for the topography (see text for a discussion). The heat flux at the base of the shallow porous layer ranges from 7.5 to 16 mW $\cdot$ m^{-2}. The black, broken line corresponds to the stereo-derived data of *Schenk and McKinnon* [2009, latitudinal profile cc' of their Figure 2]. Note that in order to make the visual comparison with our results easier, both vertical (+935 m) and horizontal (+35°) offsets have been applied to this profile (viz. the latitude axis refers only to modelled profiles). Label A ($\lambda \approx 20°$) denotes the major basin identified by *Schenk and McKinnon* [2009].

evolution timescale of 100 Ma, this value becomes 2280 m. However, apart from basin A and the major topographic bump to its south, significant discrepancies appear between the observed data and the regular, ideal topographic profiles computed in this study. These discrepancies are probably reflective of Enceladus's complex history and lithospheric structure: for instance, if the locus of high heat-flux regions has moved over time, the resulting porosity and topography pattern will be more complicated than our simple model suggests.

[22] Our model does not reproduce the south polar depression. This is because the model does not include either the high observed polar heat flux or potential thinning of the ice shell in this region. One important difference between topography caused by porosity variations and topography caused by shell thickness variations is that the former is much longer-lived. Shell thickness variations are destroyed by the lateral flow of warm, ductile ice [*Stevenson*, 2000]; porosity can persist in cold ice essentially indefinitely.

4. Discussion and Implications

[23] Figure 3 shows that shallow viscous compaction of ice induced by deeper convection can explain a significant fraction of the long-wavelength surface topography observed on Enceladus. In particular, the initial porosity required for the shallow layer is found to be 25–30%, a rather reasonable range of values for icy satellite regoliths [e.g., *Eluszkiewicz*, 1990; *Durham et al.*, 2005]. Recall also that Figure 3 compares our numerical results with the *most prominent* basin discovered by *Schenk and McKinnon* [2009]; the smaller depth of other large basins found on Enceladus might be explained by lower porosities (e.g., 15–20%).

[24] Is an initially porous layer tens of kilometers thick plausible on a differentiated body such as Enceladus? Porosity which was formed as Enceladus accreted was likely destroyed if early, rapid differentiation (e.g., due to ^{26}Al decay) took place. However, near-surface porosity could have readily been regenerated during a late heavy bombardment (LHB) episode around 3.9 Gyr B.P. As discussed in *Nimmo and Korycansky* [2012], large quantities of material were delivered to Enceladus during the LHB, likely more than enough to produce a near-surface megaregolith. Something similar appears to have happened at the Moon, where gravity measurements from the GRAIL mission indicate that a mean porosity of 12% characterizes the lunar subsurface over depths of at least several kilometers [*Wieczorek et al.*, 2013]. Alternatively, if Enceladus experienced more gradual differentiation some time after the LHB [e.g., *Pappalardo and Schubert*, 2013], then near-surface porosity generated during accretion probably remained intact. Only if Enceladus experienced energetic differentiation later than the LHB—which seems unlikely—does the assumption of a thick initially porous layer become implausible. Subsequent resurfacing events would likely have destroyed pre-existing topography and porosity, so our analysis is most applicable to the ancient, unresurfaced cratered regions of Enceladus.

[25] Another limitation of our current model is the assumption of a temperature-independent thermal conductivity. In order to check whether this additional complexity would affect our results, we have also conducted runs with the variable quantity $k(\phi, T)$ according to the empirical law of *Klinger* [1980] (see Table 1): the obtained topographic peak-to-peak amplitudes typically tend to be at least 30% greater in the case with $k(\phi, T)$, further supporting our model. The specific heat of ice also significantly varies with temperature [*Klinger*, 1981]. Accordingly, we also ran models with the variable quantity $c_p(T)$ [see Table 1]. As expected, the effects remain minor (typical variations of less than 1.5% on the topographic profiles), mainly because the variations of c_p only affect the diffusion timescale of the shallow layer ($\sim$ 10 – 30 Ma), not the final, equilibrium temperature and porosity distributions. Fully exploring these effects would require running a convection model in which the temperature-dependence of k and c_p were taken into account [e.g., *Grott et al.*, 2007], as well as the evolution of the near-surface porosity. However, the main effect of $k(\phi)$ would be a slightly thinner stagnant lid, probably not affecting our general results to a significant extent.

[26] It is worth recalling here that we only considered a pure water ice composition for the shallow layer. For instance, clathrate hydrates may be present in Enceladus's subsurface [e.g., *Kieffer et al.*, 2006]. *Schenk and McKinnon* [2009] suggested that the larger thermal expansivity of clathrates compared to water ice might explain the topographic variations associated with Enceladus's large basins. In our pore-closure model, clathrate hydrates would act mainly through their lower thermal conductivity, 0.5–0.7 $W \cdot m^{-1} \cdot K^{-1}$ [*Durham et al.*, 2010], promoting higher subsurface temperatures and greater overall compaction. This effect would oppose the thermal expansivity effect. In any event, exploring the effects of clathrate hydrates on pore compaction is beyond the scope of this paper, and is kept for future studies. In particular, the rather poorly constrained rheology of clathrate hydrate/pure ice mixtures [*Durham et al.*, 2010] would have to be considered to consistently describe pore annealing.

[27] Another limitation of our model is its two-dimensionality. In a fully three-dimensional spherical geometry, hot upwellings would form circular plumes, whereas downwellings would have sheet-like structures. The fact that the observed basins on Enceladus [*Schenk and McKinnon*, 2009; *Nimmo et al.*, 2011] are rather circular in shape is therefore entirely consistent with our model. Moreover, our main conclusions should remain unchanged, because both heat flux values and convective wavelength should not significantly differ between our 2D-spherical convection model and a fully spherical one.

[28] At first sight, our model is further supported by the existence of numerous abnormally relaxed craters on Enceladus's surface [*Smith*, 1982; *Passey*, 1983]. Indeed, basin B of *Schenk and McKinnon* [2009] (or the corresponding broad low region on the map of *Nimmo et al.* [2011]) matches well with one of the two regions inferred by *Bland et al.* [2012] to have experienced high heat fluxes on the basis of relaxed craters. Our model seems consistent with these observations because it predicts that such high heat flux regions should be associated with topographic lows.

[29] We note that *Bland et al.* [2012] inferred heat fluxes that are much higher than those characterizing stagnant lid convection in our model. They found that typical heat fluxes of at least 50 $mW \cdot m^{-2}$ (and up to 150 $mW \cdot m^{-2}$), acting over short timescales ($\sim$ 2 Ma), are required to account for

the inferred crater relaxation fractions. Such brief, high heat flux episodes in shallow regions of cratered (and initially porous) terrains will necessarily yield a significant porosity reduction, leading to subsidence. This kind of effect can be tested with our model.

[30] As an example of such a test, we fixed the surface temperature at 70 K and adopted a constant (background) heat flux of 10 mW $\cdot$ m^{-2} (close to the average value of the heat fluxes investigated above, see captions of Figures 2 and 3). For a typical grain size of 1 mm, a 0.5 Ma (stepwise) episode of enhanced heat flux (50 mW $\cdot$ m^{-2}) affecting a 10 km thick porous ice shell produced a differential topography of Δh = 1000 m after 1 Ga, assuming an initial porosity of 30%. Changing this value to ϕ_0 = 0.20, or ϕ_0 = 0.15 yields Δh = 390 m and Δh = 200 m, respectively. Thus brief, local episodes of high heat flux (e.g., upwelling of hot, possibly tidally heated material under a weakened lithosphere; [*Tobie et al.*, 2008; *O'Neill and Nimmo*, 2010]) can lead to significant amount of compaction and, therefore, to subsidence that may contribute to the formation of Enceladus's large basins. This mechanism might have acted in concert with the longer-term, large scale convection-driven compaction mechanism investigated in this paper. Note, however, that, if local upwellings reached near-surface depths, as would be the case if yielding were considered, the (transient) dynamic topography may have been larger, opposing the compaction-induced topography.

[31] A significant initial porosity (> 20%) is required in the shallow parts of Enceladus to explain the surface long-wavelength topography with our model. Because compaction-induced topography is a long-lived feature, the observed topographic basins may be remnants ("trace fossils") of various past episodes of thermal activity. An interesting outcome of this mechanism is that the associated gravity anomalies at spacecraft altitude would be negligibly small—the column mass does not vary laterally, and the thickness of the compacting layer remains very small compared to spacecraft altitude. By contrast, topography caused by variations in ice shell thickness should produce detectable gravity anomalies, because the mass excess and associated deficit are separated by the thickness of the shell.

5. Conclusions

[32] We have shown that thermal convection can be responsible for Enceladus's long wavelength topography. The mechanism we propose is viscous compaction induced in regions of high heat flux, resulting in low topography above upwellings and an absence of gravity anomalies at spacecraft altitude. For such a mechanism to occur, the existence of an initial shallow porous layer (i.e., megaregolith) is required. An initial porosity on the order of 20–30% is sufficient to explain both the amplitude and the wavelength of the topographic depressions observed by *Schenk and McKinnon* [2009] and *Nimmo et al.* [2011]. Enceladus's large surface basins may be remnants of one or several episodes of past thermal activity. Because the porosity structure is long-lived, even old and currently inactive regions of Enceladus, and perhaps other icy satellites, may record signs of ancient activity and heating. The compaction mechanism proposed in this study works best in low-gravity environments where convection has occurred; Enceladus and (perhaps) Miranda [*Thomas et al.*, 1987; *Janes and Melosh*, 1988] are probably the most likely examples.

[33] **Acknowledgments.** This research is supported by NASA grants NNX11AK44G, NAS2-03144 and the CDAPS program to FN, and NASA grant NNX12AK44G to JHR. The portion of this work performed by RTP was performed under a contract with the NASA. The authors thank the editor, M.A. Wieczorek, and two anonymous reviewers for their comments that helped improve the manuscript.

References

Barr, A. C., and W. B. McKinnon (2007), Convection in Enceladus ice shell: Conditions for initiation, *Geophys. Res. Lett.*, *34*, L09202, doi:10.1029/2006GL028799.

Bland, M. T., K. N. Singer, W. B. McKinnon, and P. M. Schenk (2012), Enceladus' extreme heat flux as revealed by its relaxed craters, *Geophys. Res. Lett.*, *39*, L17204, doi:10.1029/2012GL052736.

Běhounková, M., G. Tobie, G. Choblet, and O. Čadek (2012), Tidally-induced melting events as the origin of south-pole activity on Enceladus, *Icarus*, *219*, 655–664, doi:10.1016/j.icarus.2012.03.024.

Castillo-Rogez, J. C., D. L. Matson, C. Sotin, T. V. Johnson, J. I. Lunine, and P. C. Thomas (2007), Iapetus' geophysics: Rotation rate, shape, and equatorial ridge, *Icarus*, *190*, 179–202, doi:10.1016/j.icarus.2007.02.018.

Collins, G. C., and J. C. Goodman (2007), Enceladus' south polar sea, *Icarus*, *189*, 72–82, doi:10.1016/j.icarus.2007.01.010.

Durham, W. B., W. B. McKinnon, and L. A. Stern (2005), Cold compaction of water ice, *Geophys. Res. Lett.*, *32*, L18202, doi:10.1029/2005GL023484.

Durham, W. B., O. Prieto-Ballesteros, D. L. Goldsby, and J. S. Kargel (2010), Rheological and thermal properties of icy materials, *Space Sci. Rev.*, *153*, 273–298, doi:10.1007/s11214-009-9619-1.

Eluszkiewicz, J. (1990), Compaction and internal structure of Mimas, *Icarus*, *84*, 215–225, doi:10.1016/0019-1035(90)90167-8.

Eluszkiewicz, J. (2004), Dim prospects for radar detection of Europa's ocean, *Icarus*, *170*, 234–236, doi:10.1016/j.icarus.2004.02.011.

Fowler, A. C. (1985), A mathematical model of magma transport in the asthenosphere, *Geophys. Astro. Fluid.*, *33*, 63–96, doi:10.1080/03091928508245423.

Goldsby, D. L., and D. L. Kohlstedt (2001), Superplastic deformation of ice: Experimental observations, *J. Geophys. Res.*, *106*, 11017–11030, doi:10.1029/2000JB900336.

Grott, M., F. Sohl, and H. Hussmann (2007), Degree-one convection and the origin of Enceladus' dichotomy, *Icarus*, *191*, 203–210, doi:10.1016/j.icarus.2007.05.001.

Janes, D. M., and H. J. Melosh (1988), Sinker tectonics: An approach to the surface of Miranda, *J. Geophys. Res.*, *93*, 3127–3143, doi:10.1029/JB093iB04p03127.

Kieffer, S. W., X. Lu, C. M. Bethke, J. R. Spencer, S. Marshak, and A. Navrotsky (2006), A clathrate reservoir hypothesis for Enceladus' south polar plume, *Science*, *314*, 1764–1766, doi:10.1126/science.1133519.

Kirchoff, M. R., and P. Schenk (2009), Crater modication and geologic activity in Enceladus' heavily cratered plains: Evidence from the impact crater distribution, *Icarus*, *202*, 656–668, doi:10.1016/j.icarus.2009.03.034.

Klinger, J. (1980), Influence of phase transition of ice on the heat and mass balance of comets, *Science*, *209*, 271–272, doi:10.1126/science.209.4453.271.

Klinger, J. (1981), Some consequences of a phase-transition of water ice on the heat-balance of comet nuclei, *Icarus*, *47*, 320–324, doi:10.1016/0019-1035(81)90179-2.

Kossacki, K. J., and J. Leliwa-Kopystyński (1993), Medium-sized icy satellites: Thermal and structural evolution during accretion, *Planet. Space Sci.*, *41*, 729–741, doi:10.1016/0032-0633(93)90115-I.

Leliwa-Kopystyński, J., and K. J. Kossacki (2000), Evolution of porosity in small icy bodies, *Planet. Space Sci.*, *48*, 727–745, doi:10.1016/S0032-0633(00)00038-6.

Leliwa-Kopystynski, J., and N. Maeno (1993), Ice/rock porous mixtures: Compaction experiments and interpretation, *J. Galciology*, *39*, 643–655.

Leliwa-Kopystyński, J., and K. J. Kossacki (1995), Kinetics of compaction of granular ices, H_2O, CO_2 and $(NH_3)_x(H_2O)_{1-x}$ at pressures of 2–20 MPa and in temperatures of 100–270 K. Application to the physics of the icy satellites, *Planet. Space Sci.*, *43*, 851–861, doi:10.1016/0032-0633(94)00215-D.

Meyer, J., and J. Wisdom (2008), Episodic volcanism on Enceladus: Application of the Ojakangas-Stevenson model, *Icarus*, *198*, 178–180, doi:10.1016/j.icarus.2008.06.012.

Nimmo, F., R. T. Pappalardo, and B. Giese (2003), On the origin of band topography, Europa, *Icarus*, *66*, 21–32, doi:10.1016/j.icarus.2003.08.002.

Nimmo, F., B. G. Bills, and P. C. Thomas (2011), Geophysical implications of the long-wavelength topography of the Saturnian satellites, *J. Geophys. Res.*, *116*, E11001, doi:10.1029/2011JE003835.

Nimmo, F., and D. G. Korycansky (2012), Impact-driven ice loss in outer Solar System satellites: Consequences for the Late Heavy Bombardment, *Icarus*, *219*, 508–510, doi:10.1016/j.icarus.2012.01.016.

Ojakangas, G. W., and D. J. Stevenson (1986), Episodic volcanism of tidally heated satellites with application to Io, *Icarus*, *66*, 341–358, doi:10.1016/0019-1035(86)90163-6.

Ojakangas, G. W., and D. J. Stevenson (1989), Thermal state of an ice shell on Europa, *Icarus*, *81*, 220–241, doi:10.1016/0019-1035(89)90052-3.

O'Neill, C., and F. Nimmo (2010), The role of episodic overturn in generating the surface geology and heat flow on Enceladus, *Nat. Geosci.*, *3*, 88–91, doi:10.1038/ngeo731.

Pappalardo, R. T., and G. Schubert (2013), Enceladus and Miranda: Similar histories of low-order convection and reorientation during differentiation, *Proc. Lunar Planet Sci. Conf.*, *44*, 2808.

Passey, Q. R. (1983), Viscosity of the lithosphere of Enceladus, *Icarus*, *53*, 105–120, doi:10.1016/0019-1035(83)90024-6.

Porco, C. C., et al. (2006), Cassini observes the active south pole of Enceladus, *Science*, *311*, 1393–1401, doi:10.1126/science.1123013.

Prialnik, D., J. Benkhoff, and M. Podolak (2004), Modeling the structure and activity of comet nuclei, in *Comets II*, edited by M. C. Festou, H. U. Keller, and H. A. Weaver, pp. 359–387, University of Arizona Press, Tucson, Ariz.

Roberts, J. H., and F. Nimmo (2008a), Near-surface heating on Enceladus and the south polar thermal anomaly, *Geophys. Res. Lett.*, *35*, L09201, doi:10.1029/2008GL033725.

Roberts, J. H., and F. Nimmo (2008b), Tidal heating and the long-term stability of a subsurface ocean on Enceladus, *Icarus*, *194*, 675–689, doi:10.1016/j.icarus.2007.11.010.

Schenk, P. M., and W. B. McKinnon (2009), One-hundred-km-scale basins on Enceladus: Evidence for an active ice shell, *Geophys. Res. Lett.*, *36*, L16202, doi:10.1029/2009GL039916.

Schubert, G., J. D. Anderson, B. J. Travis, and J. Palguta (2007), Enceladus: Present internal structure and differentiation by early and long-term radiogenic heating, *Icarus*, *188*, 345–355, doi:10.1016/j.icarus.2006.12.012.

Shoshany, Y., D. Prialnik, and M. Podolak (2002), Monte Carlo modeling of the thermal conductivity of porous cometary ice, *Icarus*, *157*, 219–227, doi:10.1006/icar.2002.6815.

Smith, B. A., et al. (1982), A new look at the Saturn system—The Voyager 2 images, *Science*, *215*, 504–537, doi:10.1126/science.215.4532.504.

Spencer, J. R., J. C. Pearl, M. Segura, F. M. Flasar, A. Mamoutkine, P. Romani, B. J. Buratti, A. R. Hendrix, L. J. Spilker, and R. M. C. Lopes (2006), Cassini encounters Enceladus: Background and the discovery of a south polar hot spot, *Science*, *311*, 1401–1405, doi:10.1126/science.1121661.

Spencer, J. R., A. C. Barr, L. W. Esposito, P. Helfenstein, A. P. Ingersoll, R. Jaumann, C. P. McKay, F. Nimmo, and J. H. Waite (2009), Enceladus: An active cryovolcanic satellite, in *Saturn From Cassini-Huygens*, edited by M. K. Dougherty, L. W. Esposito, and S. M. Krimigis, pp. 683–724, Springer, Dordrecht, The Netherlands.

Stevenson, D. J. (2000), Limits on the variation of thickness of Europa's ice shell, *Lunar Planet Sci.*, *XXXI*, Abstract 1506.

Thomas, P. J., R. T. Reynolds, S. W. Squyres, and P. M. Cassen (1987), The viscosity of Miranda, *Proc. Lunar Planet Sci. Conf.*, *18*, 1016.

Tobie, G., O. Čadek, and C. Sotin (2008), Solid tidal friction above a liquid water reservoir as the origin of the south pole hotspot on Enceladus, *Icarus*, *196*, 642–652, doi:10.1016/j.icarus.2008.03.008.

Wieczorek, M. A., et al. (2013), The crust of the Moon as seen by GRAIL, *Science*, *339*, 671–675, doi:10.1126/science.1231530.

Zhang, K., and F. Nimmo (2009), Recent orbital evolution and the internal structures of Enceladus and Dione, *Icarus*, *204*, 597–609, doi:10.1016/j.icarus.2009.07.007.